The characteristics of air pollution induced by the quasi-stationary front: Formation processes and influencing factors

Xin Wu [a,c], Mengren Li [a], Jinsheng Chen [a,*], Hong Wang [d], Lingling Xu [a], Youwei Hong [a], Guoqing Zhao [a], Baoye Hu [a,c], Yanru Zhang [a,c], Yangbin Dan [a], Shaocai Yu [b,*]

[a] Center for Excellence in Regional Atmospheric Environment, Institute of Urban Environment, Chinese Academy of Sciences, Xiamen 361021, PR China
[b] Research Center for Air Pollution and Health, Key Laboratory of Environmental Remediation and Ecological Health, Ministry of Education, College of Environment and Resource Sciences, Zhejiang University, Hangzhou, Zhejiang 310058, PR China
[c] University of Chinese Academy of Sciences, Beijing 100049, PR China
[d] Fujian Institute of Meteorological Sciences, Fuzhou 350001, PR China

HIGHLIGHTS

- An air pollution episode induced by quasi-stationary front was diagnosed.
- Free H^+ hydrolysis from HSO_4^- played a key role in triggering the air pollution.
- Homogeneous and heterogeneous reactions both occurred via liquid water.

GRAPHICAL ABSTRACT
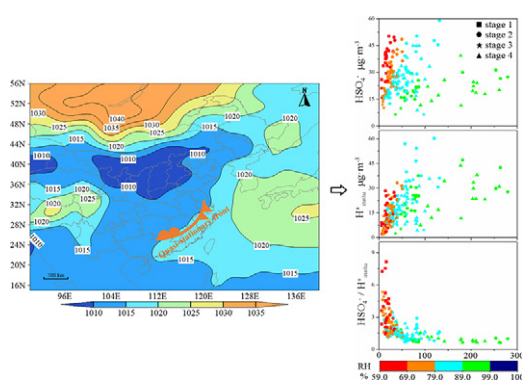
ARTICLE INFO

ABSTRACT

The quasi-stationary front is a significant weather system which influences East Asia in spring. The air quality deteriorated along with the moist circumstance when the quasi stationary front dominated the area. Surface meteorological parameters, air pollutants and $PM_{2.5}$ chemical species were observed during the air pollution episode. Liquid water content and aerosol acidity were calculated by thermodynamic model in order to investigate heterogeneous/aqueous reactions for secondary aerosol formation. The episode was divided into four stages based on quasi-stationary front influences. Hourly $PM_{2.5}$ concentrations were up to 150.2 μg·m^{-3} while O_3 concentrations reached the minimum value of 1.27 μg·m^{-3}, indicating that the precursor gas NOx participated in the different reactions during the episode. Nitrate proportion of water-soluble inorganic ions was 42.2%. High concentrations of secondary inorganic aerosol ions and the high sulfur oxidation ratio (SOR) and nitrogen oxidation ratio (NOR) indicated the increasing conversions from SO_2 and NOx to their corresponding particulate phases. Ratios of $[NO_3^-]/[SO_4^{2-}]$ and $[NH_4^+]/[SO_4^{2-}]$ in the four stages declared that nitrate formation preferred heterogeneous conversions. A series of liquid water content (LWC) fitting equations between relative humidity

* Corresponding authors.
  E-mail addresses: jschen@iue.ac.cn (J. Chen), shaocaiyu@zju.edu.cn (S. Yu).

Liquid water content

and inorganic ions were conducted to verify heterogeneous aqueous reactions of NO_2 and secondary nitrate formation. The results of this study highlighted the significance of LWC and chemical reactions associated with acidity during the specific synoptic situation in South China.

1. Introduction

The air pollution caused by fine particulates ($PM_{2.5}$), has plagued China for a few decades. The effects of air pollution include poor visibility, radiative balance alter of atmosphere, global climate change and human health risks (Watson, 2002; Ramanatha et al., 2001; Pope, 2000). The associated pollutants are emitted from anthropogenic and natural sources, then possibly secondarily formed with chemical and photo-chemical reactions, but pollution is basically dominated by specific synoptic situations. Numerous studies have revealed the relationships between air pollution episodes and synoptic situations (Kalkstein and Corrigan, 1986; Greene et al., 1999; Zhang et al., 2015). Long regional transport of $PM_{2.5}$ by invoking the relatively stagnant air masses was one of the major sources for severe air pollutions (Li et al., 2015). High concentrations of pollutants were found in stable air masses or under strong anticyclone control, whereas low concentrations occurred in moist unstable air masses (Davis and Kalkstein, 1990). The air pollution episodes always aroused public and scientists' attentions. Numerous studies on air pollution episodes have been conducted in terms of synoptic situations and formation mechanisms of particulate matters (Greene et al., 1999; Chen et al., 2008; Bei et al., 2016).

Climate in South China belongs to the monsoon of subtropical moist marine climate zone. In March and April, cold air from north and warm moist air from south are quite implicitly promising, resulting in quasi-stationary front which lies on South China. Gradients of air pressure were lesser and the circumstance was stable with low wind speed, which provides proper conditions for the air pollution episode formations probably. The phenomenon often occurred between 22 N–26°N. However, previous studies focused on the weather caused by quasi-stationary front, especially for the precipitation (Li et al., 2017; Wang et al., 2018). In this paper, the moist phenomenon and quasi-stationary front locations were the concerns which could induce the air pollution with adequate water vapor. A subtropical city in southeast China, Xiamen was selected appropriately to study the role of quasi-stationary fronts in determining the air pollution episodes.

This paper will attempt to explore the synoptic situations and formation mechanisms for air pollution associated with the formation of the quasi-stationary front. The main purposes of this study are two folds: the first is to establish the connection between air pollution and quasi-stationary front position. The second is to understand the mechanisms of air pollution via homogeneous gaseous and/or heterogeneous aqueous reactions. As far as we know, this study is the first to focus on the air pollution caused by a well-defined quasi-stationary front. The observation site is set up on the roof top of one building located in Institute of Urban Environment, Chinese Academy of Sciences (24°36′N, 118°3′E), Xiamen, China. There is no industrial source nearby and the site is representative of urban environment (Wu et al., 2019).

2. Materials and methods

2.1. Observed data

Online hourly $PM_{2.5}$ mass concentrations were measured by a tapered element oscillating microbalance (TEOM1405, Thermo Scientific Corp., MA, US). Visibility was monitored by the Belfort Model 6000 Visibility Sensor (Belfort Instrument Corp., MD, US). Trace O_3, SO_2, NO-NO_2-NOx and CO gases were determined by a resolution of 1 h by applying online Thermo Instruments TEI 49i, 43i, 42i, and 48i, respectively.

Ambient meteorological parameters including temperature (T), relative humidity (RH), surface pressure (P), wind speed (WS) and wind direction (WD) were determined by an ultrasonic atmospherium (150WX, Airmar, the USA).

Water-soluble inorganic ions (WSIIs) of $PM_{2.5}$ including SO_4^{2-}, NO_3^-, NH_4^+ and other ions in ambient air were measured by Monitor for AeRosol and GAses (MARGA) with one-hour resolution. Details on the MARGA are given elsewhere (Trebs et al., 2004). Ultraviolet (UV) radiation is part of the Sun's light spectrums that reach the earth. A UV radiometer (SUV5) was applied to monitor the total UV irradiance. $J_{(NO2)}$ filter radiometer was also utilized in this paper to quantify the photolysis rates of in-situ NO_2 in the atmosphere.

2.2. Thermodynamic model

E-AIM IV (Extended Aerosol Inorganic Model IV version) is a community model for calculating gas/liquid/solid partitioning in aerosol systems containing inorganic and organic components, water, solute and solvent activities in aqueous solutions and liquid mixtures (http://www.aim.env.uea.ac.uk/aim/aim.php). The inorganic element of E-AIM IV is an equilibrium thermodynamic model of the system (Clegg et al., 1998; Friese and Ebel, 2010). The E-AIM IV can be used to simulate gas/aerosol partitioning processes and calculate the equilibrium composition of the aqueous phase or solid aerosol phase. E-AIM IV is a state-of-the-art model that can accurately simulate the aqueous and solid phases of ionic compositions in the mixing system (H^+-NH_4^+-SO_4^{2-}-NO_3^--Cl^--Na^+-H_2O) at a given temperature (T) and relative humidity (RH). The hourly averaged T, RH, SO_4^{2-}, NO_3^-, Cl^-, NH_4^+, Na^+ and molar concentrations of total aerosol acidity (H_{total}^+) were used as the input in the model E-AIM IV to obtain the concentrations of free ions (including free H^+ (H_{insitu}^+) and HSO_4^- in the aqueous phase, and any salt of these ions that were formed in the solid phase at equilibrium, as well as liquid water content (LWC). H_{insitu}^+, defined as the moles of free hydrogen ions in the aqueous phase of aerosols per unit of air (nmol·m^{-3}), is the actual acidity in the droplets of the aerosols. The H_{total}^+ was estimated from the ionic balance of the relevant ionic species:

$$H_{total}^+ = 2 \times SO_4^{2-} + NO_3^- + Cl^- - NH_4^+ - Na^+ \qquad (1)$$

Based on the outputs of E-AIM IV, the pH of aerosol was calculated as follow:

$$pH = -\lg\left(\frac{\gamma \times H_{insitu}^+}{V_{aq}/1000}\right) \qquad (2)$$

where γ and V_{aq} denote the activity coefficient and the volume of particle aqueous phase in air (cm^3·m).

The forward mode of ISORROPIA II thermodynamic model (http://isorropia.eas.gatech.edu) was employed to compute the equilibrium composition in the aerosol system (Fountoukis and Nenes, 2007). The results of LWC were used to compare with that of E-AIM IV. ISORROPIA II was run by assuming that aerosol solutions were metastable (only a liquid phase) (Bougiatioti et al., 2016; Guo et al., 2016). The pH values from ISORROPIA II were calculated using the following equation:

$$pH = -\lg\left(\frac{1000 \times H^+}{LWC}\right) \qquad (3)$$

where H^+ is the equilibrium particle hydronium ion concentration per volume air.

2.3. Synoptic chart

The synoptic situation is the distribution and characteristics of weather systems. The synoptic charts could reveal the atmospheric and circulation status. The synoptic situations at different layers were unity and restricted. In this paper, the synoptic charts were obtained from Korea Meteorological Administration (http://web.kma.go.kr/eng/weather/images/analysischart.jsp).

2.4. Aqua MODIS

The Moderate Resolution Imaging Spectroradiometer (MODIS) sensor is one of the key instruments on the Terra and Aqua platforms. The Aqua MODIS cloud imaginaries were used in the manuscript to recognize the locations of the quasi-stationary front. Radiance calibration products of MYD02 were employed and its resolution was 1×1 km.

2.5. Backward trajectory

To confirm the air mass trajectories and locations of the quasi-stationary front, the Hybrid Single-Particle Lagrangian Integrated Trajectory (HYSPLIT) model was used to calculate 72-hour backward trajectories in this study. The trajectory cluster analyses were based on the GIS-based software TrajStat (Wang et al., 2009). The gridded input meteorological data were from the Global Data Assimilation System (GDAS).

3. Results

3.1. Synoptic situation

Fig. 1 demonstrates the variations of synoptic situations during the episode. Surface, 850 hPa and 500 hPa layers corresponded to low, medium and high levels, respectively. Six key times (i.e. 8:00 on 10 Mar, 8:00 on 13 Mar, 8:00 on 14 Mar, 20:00 on 17 Mar, 8:00 on 18 Mar and 8:00 on 19 Mar) were selected to recognize the quasi-stationary front locations and uniform pressure fields. The cold high was running into sea at 2:00 on 10th March as well as south trough at 500 hPa layer, indicating that cold air masses from north was about to cease transportation while the wind speed decreased. Xiamen was in front of the South Trough where convergence and updrafts occurred. South trough probably offered adequate water vapor and dynamic conditions. At 8:00 on 13th March, the air flows from northeast and southeast converged and the quasi-stationary front was formed in south China. The quasi-stationary front barely moved from 13th to 14th March and this could be used to testify the existence and location of the quasi-stationary front. No obvious wind shear near Xiamen at 850hpa was observed because the atmosphere stayed stable. The air was cut by southwest flow in midlatitude so that a low vortex center of cold air was formed in the vicinity of North China at the level of 850 hPa. Uniform pressure fields also emerged at the surface layer so the wind speed was low and the wind direction was changeable. The quasi-stationary front started to move southward since 17th March and surface wind direction changed to southeast. Cold front dominated the area in fact. The quasi-stationary front appeared again in 18th March and synoptic situations fluctuated seldomly. Until 8:00 on 19th March, uniform pressure fields still occupied the area and south trough started to move eastward. The synoptic situations diagnosis revealed the circumstance with moist steam. When the temperature approached to dew point temperature, water vapor in the air tended to saturate humidity and generate liquid water on the surfaces of particles (Zhao et al., 2015a; Zhao et al., 2015b; Park and Kim, 2004).

As vividly illustrated in Fig. 2, cloud systems changed from the beginning of this episode. It was cloudless in Fig. 2(a) when the cold front governed the area. Banded cloud systems arose in 12th March and the cloud lied on the north of the observation site. In 13th March the cloud system evolved and enhanced, and this could reveal the quasi-stationary front location to some extent. Cloud system covered the area from 14th to 19th March gradually with possible occurred precipitation or water vapor. Water vapor would not be blown away or lifted to cloud. Cold air underlying surface was encountered with warm moist flow that promoted water condensation to accelerate the formations of the air pollution episode. Fig. 3 depicted the trajectories and clusters during the air pollution episode. The trajectories and clusters from north and south converged near the observation site, especially in the southeast of China. The air masses encounter and convergence reflected that the quasi-stationary front was located in this place.

3.2. Overview of the air pollution

Time series of surface parameters including meteorological and pollution parameters are illustrated in Fig. 4. Wind directions changed along with synoptic situation variations as indicated in Fig. 1. Temperature rose from stage 1 to stage 2, then dropped in stage 3 and rose again in stage 4. Atmosphere pressure trends basically reversed temperature, revealing passages of the cold front. Ambient relative humidity indicated atmospheric water vapor saturation which influenced aerosol formation directly. Precipitation in stages 2 and 4 caused 100% RH. In general, RH was at relative high level during this episode (80.32% in average). Visibility varied from time to time and appeared opposite trend with RH. There were 13 periods with visibility below 10 km. The decline of visibility was influenced by both cold air from north and warm moist air from southwest as well as the enhancement of temperature and relative humidity.

Hourly $PM_{2.5}$ concentrations reached the maximum value of 150.2 $\mu g \cdot m^{-3}$ at 10:00, 15th March. Daily average $PM_{2.5}$ concentration was up to 62.14 $\mu g \cdot m^{-3}$, which exceeded the first grade of the Chinese National Ambient Air Quality Standard for daily averaged $PM_{2.5}$ concentrations (CNAAQS, GB3095-2012, 35 $\mu g/m^3$). Chemical composition of atmospheric $PM_{2.5}$ is very complex, including sulfate, nitrate, ammonium (SNA), organic carbon, inorganic carbon and metal elements. The water-soluble inorganic ions (WSIIs) are the major components of $PM_{2.5}$ and determine the evolution of $PM_{2.5}$. In this study, the average mass concentrations of WSIIs and SNA, which were 28.95 and 26.60 $\mu g/m^3$, respectively, were very similar through the episode. WSIIs and SNA tendencies matched perfectly with those of $PM_{2.5}$. WSIIs accounted for 48.36% of the $PM_{2.5}$, and SNA accounted for 44.56% of $PM_{2.5}$ and 90.15% of the WSIIs during the periods. The episode with nitrate proportion of WSIIs up to 42.2%, was defined as high-nitrate episode. Hourly O_3 trends were opposite to $PM_{2.5}$ indicating that precursors of NOx (NO+NO$_2$) reactions occurred in both O_3 and $PM_{2.5}$ formations. NO-NO$_2$-NOx, CO and SO$_2$ showed similar tendencies with $PM_{2.5}$ also revealing that the air pollution was possibly influenced by local emissions. Local emissions affected the air pollutant variation along with the synoptic situations.

The sulfur oxidation rate (SOR) and nitrogen oxidation rate (NOR) were defined as followed (Kaneyasu et al., 1995):

$$SOR = \frac{nss\ SO_4^{2-}}{nss\ SO_4^{2-} + SO_2} \tag{4}$$

$$NOR = \frac{nss\ NO_3^-}{nss\ NO_3^- + NO_2} \tag{5}$$

where nss denotes non-sea-salt of the species. As the indicators of secondary transformation processes, high SOR and NOR values manifested the high rates of conversions from gases to secondary particles (Sun
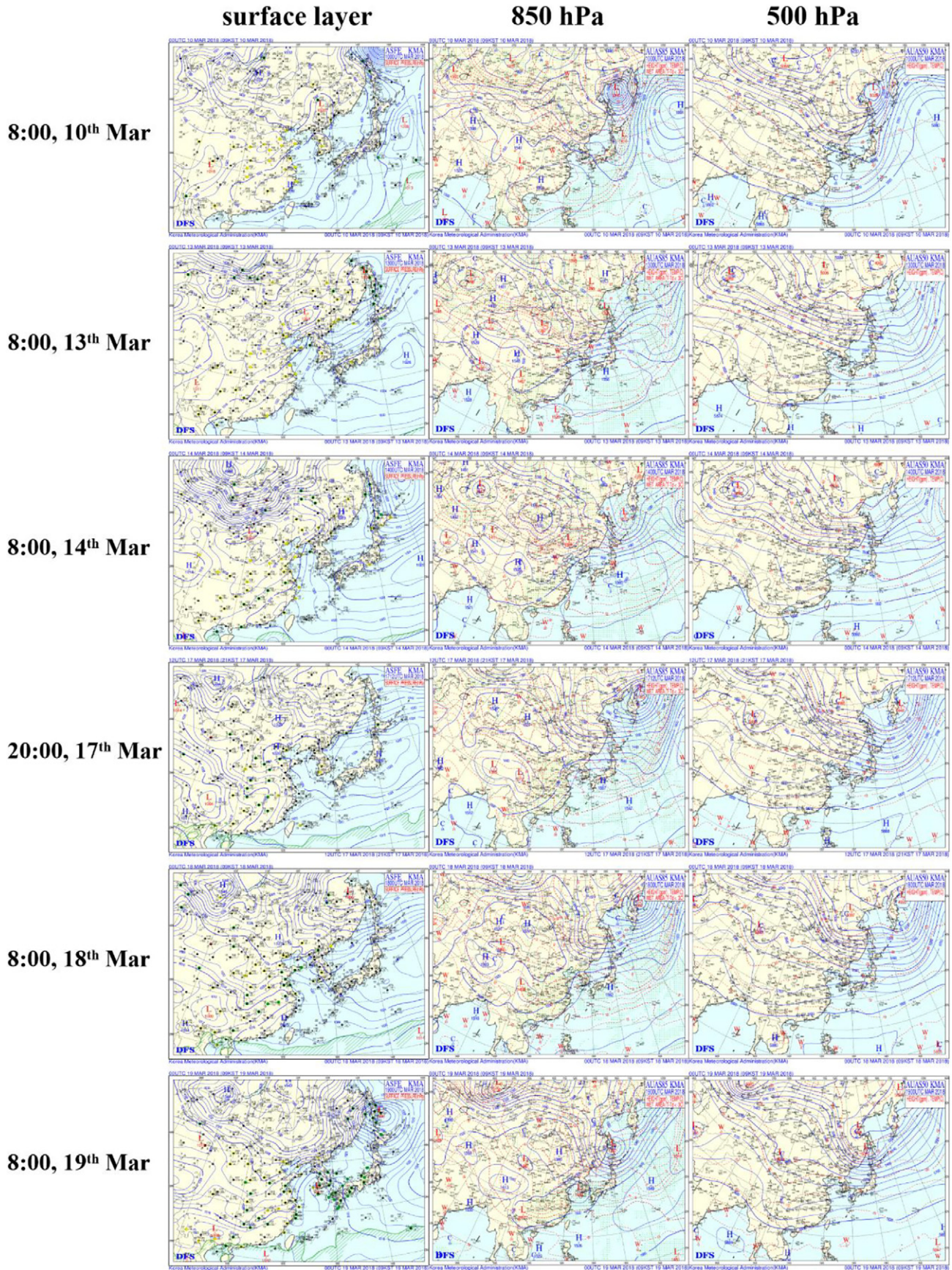
surface layer **850 hPa** **500 hPa**

8:00, 10th Mar

8:00, 13th Mar

8:00, 14th Mar

20:00, 17th Mar

8:00, 18th Mar

8:00, 19th Mar

Fig. 1. Synoptic situations at surface, 850 hPa and 500 hPa layers during the air pollution episode.
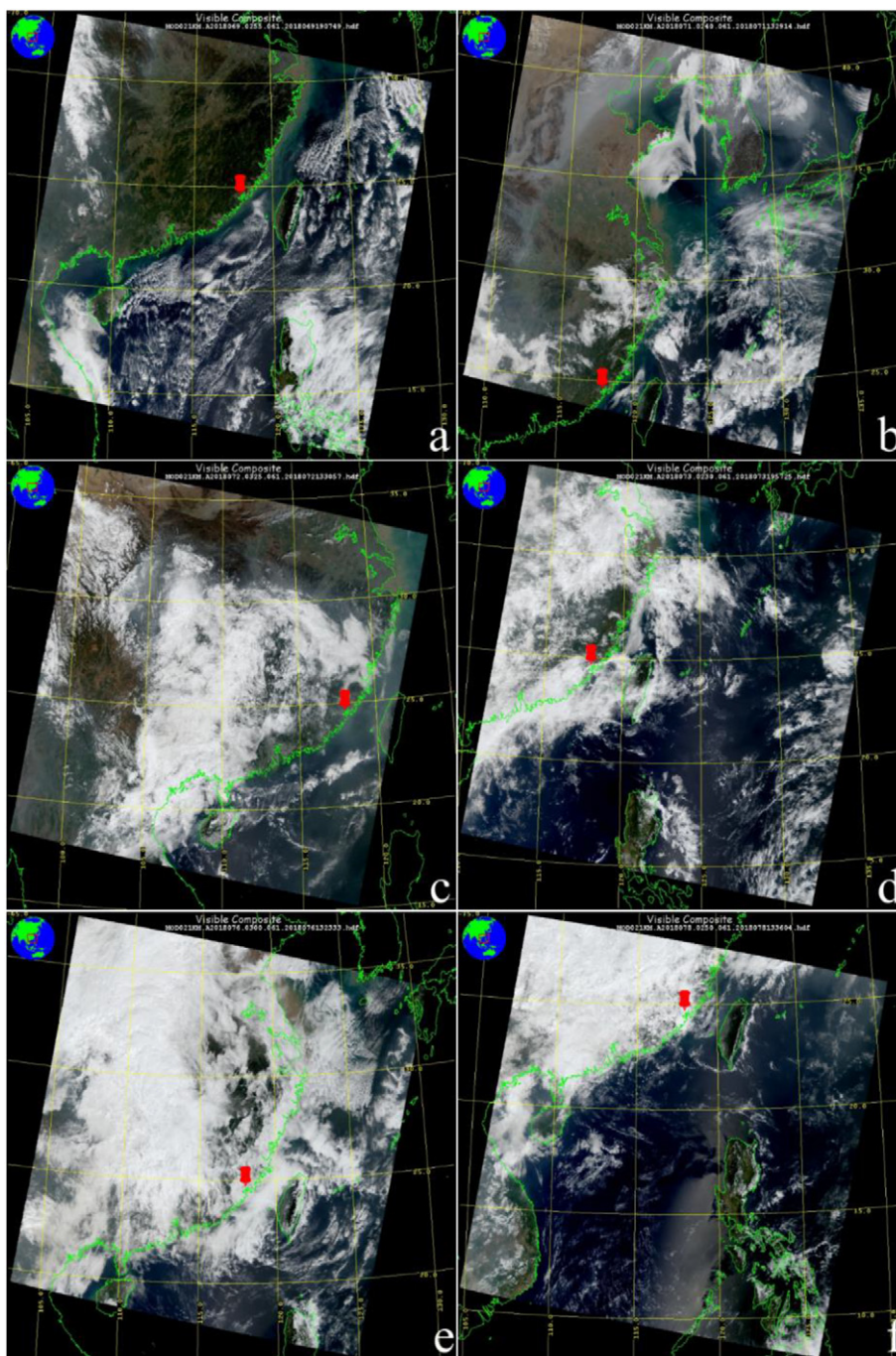
Fig. 2. MODIS images of the banded cloud systems evolution during the episode. The red dot is the location of the observation site (a: 8:55, 10th Mar; b: 10:40, 12th Mar; c: 11:25, 13th Mar; d: 10:30, 14th Mar; e: 11:00, 17th Mar; f: 10:50, 19th Mar. The time was corresponding to local time.)

et al., 2006; Tian et al., 2017). Nevertheless, SOR and NOR were at relative low levels in this study. Average values of SOR and NOR were 0.35 and 0.15, respectively. Sulfur oxidation is the main pathway of SO_2 conversion while NOx has two conversion pathways: photo-chemical reactions of decomposition O radicals to participate O_3 formation and oxidation to nitrate via homogeneous gas and/or heterogeneous aqueous reactions (Ge et al., 2013; Wang et al., 2019).

3.3. Stages division

The episode was divided into four stages according to the quasi-stationary front locations. Stage 1 was from the beginning to 14:00,

11th March, when the cold front dominated the area; stage 2 was from 15:00, 11th to 14:00, 16th March when the quasi-stationary front appeared; stage 3 began from 15:00, 16th to 20:00, 17th March when the cold front governed this area again; quasi-stationary front repeated apparently from 21:00 to the end that was classified to stage 4. The observed parameters in the four stages were vividly demonstrated in Table 1. Obviously, the characteristics of most parameters and species in stages 1 and 3 were similar while those in stages 2 and 4 were similar, but the differences between stages 1 and 3, and stages 2 and 4 are clearly depicted. For example, temperature was lower in stages 1 and 3 dues to the cold front dominations, while in stages 2 and 4, temperature was at
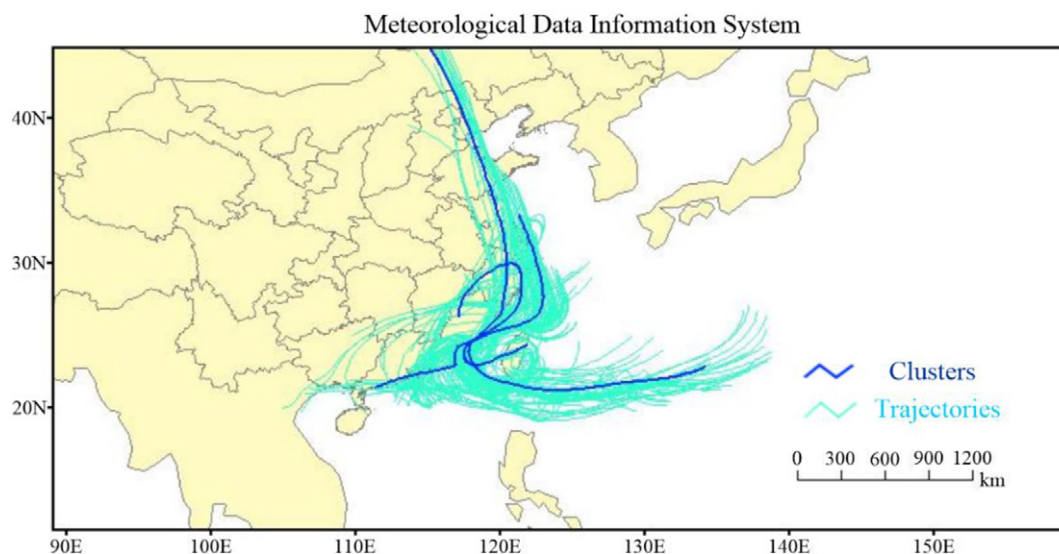
Fig. 3. 72-hour back trajectories and clusters during the air pollution episode.

relatively high levels. RH and P showed opposite trends in four stages totally. RH in stages 2 and 4 were affected by quasi-stationary fronts which could humidified circumstance and furthermore, the precipitation made the atmosphere moister. Air pressure tendencies along with temperature corresponding to the synoptic situations indicate the passages of cold front. The quasi-stationary fronts appeared in stages 2 and 4 when cold and warm air masses confronted each other. Northerly wind prevailed in stages 1 and 3 while easterly wind and breeze possessed in stages 1 and 3.

Table 1 also shows that in stages 2 and 4, not only the hourly average mass concentrations of $PM_{2.5}$ significantly increased along with visibility decrease, but also WSIIs and SNA increased more than those in stages 1 and 3, demonstrating the enhanced formation of SNA in the haze episodes. The result is consistent with the previous studies (Wang et al., 2016a; Wang et al., 2016b). Moreover, SNA proportions of $PM_{2.5}$ were between 0.41 and 0.49, indicating that the enhanced formation of SNA played a crucial role in inducing the occurrence and evolution of this episode, especially in stages 2 and 4 (Liu et al., 2016). SOR and NOR are two vital index which indicate the formation processes and pathways of sulfate and nitrate. In this study, SOR and NOR were both slightly lower in stages 2 and 4 than those in stages 1 and 3. Previous studies reveals that high SOR and NOR along with the high level of particle water content could elucidate the heterogeneous aqueous reactions for the nitrate formation (Kong et al., 2018). Nevertheless, the differences of SOR and NOR among the four stages were small, which could not testify the pathways of particles entirely.

4. Discussion

4.1. The potential pathways of sulfate and nitrate formation

An increasing number of high-nitrate air pollution episodes are observed in China in recent years, and therefore more and more attentions have been paid to the formation of nitrate. The nitrate formation in the atmosphere is complicated, and many factors influenced the formation mechanisms of nitrate, such as temperature, RH, ammonium availability, aerosol acidity, liquid water and the preexisting particles (Pathak et al., 2009; Tian et al., 2017). There are two major pathways for the formation mechanisms of particulate nitrate. The first pathway is that nitric acid reacts with

ammonia to form NH_4NO_3 in the aerosol phase:

$$HNO_{3(g)} + NH_{3(g)} \Longleftrightarrow NH_4NO_{3(s,aq)} \tag{6}$$

The second pathway is the hydrolysis of N_2O_5, which is the major channel of nitrate formation during nighttime hours:

$$N_2O_{5(aq)} + H_2O_{(aq)} \rightarrow 2HNO_{3(aq)} \tag{7}$$

It is noted that the increased heterogeneous production of nitrate in nighttime needed hygroscopicity active (Yan et al., 2017). In this study, the average temperature and RH were 16.84 °C and 80.32%, respectively (Table 1). The high RH contributed to the heterogeneous aqueous reactions of SO_2 and NO_2, especially in the high-nitrate air pollution episodes as discussed above. Meanwhile, high RH could make gaseous HNO_3 and NH_3 be dissolved in humid PM, and hence enhance particulate NO_3^- and NH_4^+ levels in the atmosphere (Trebs et al., 2004). The low temperature would contribute to the stability of the formed NH_4NO_3 because the formed NH_4NO_3 is thermodynamically unstable. Considering the existence of heterogeneous aqueous reactions, in this section, the existing forms of sulfate and nitrate in $PM_{2.5}$ are briefly discussed.

Fig. 5 exhibited the scatter plots of $[NO_3^- + 2 \times SO_4^{2-}]$ vs. $[NH_4^+]$, $[NO_3^-]/[SO_4^{2-}]$ vs. $[NH_4^+]/[SO_4^{2-}]$ and $[NO_3^-]$ vs. excess $[NH_4^+]$ with RH gradient in the four stages. The excess NH_4^+ were considered to neutralize NO_3^-. In this study, the excess NH_4^+ was defined as excess $[NH_4^+] = ([NH_4^+]/[SO_4^{2-}] - 2) \times [SO_4^{2-}]$. The concentration of nitrate increased with excess ammonia, which implied that in the ammonium-rich samples nitrate would be formed via the gas-phase homogeneous reaction $HNO_{3(g)} + NH_{3(g)} \leftrightharpoons NH_4NO_{3(s,\ aq)}$ when $[NH_4^+]/[SO_4^{2-}] > 2$. The ratios in the four stages of $[NO_3^- + 2 \times SO_4^{2-}]$ and $[NH_4^+]$ were varied from 1.03–1.10, which indicated the good ion balance and a little acid in the hourly samples. The distributions of scatters in stages 1 and 3 concentrated at the low levels while the other scatters in stages 2 and 4 were more discrete, as well as the distributions with different RH gradients. The scatters in stages 1 and 3 are at low levels in Fig. 5(a) and (c), because the distributions of scatters were determined directly by the concentrations of $[NO_3^-]$, $[SO_4^{2-}]$ and $[NH_4^+]$, which induced the differences between stages 1 and 3, and stages 2 and 4. In Fig. 5(b), the molar ratios scatters of $[NO_3^-]/[SO_4^{2-}]$ and $[NH_4^+]/[SO_4^{2-}]$ were mixed in four stages. In stage 3, the molar ratios of $[NO_3^-]/[SO_4^{2-}]$ and $[NH_4^+]/$
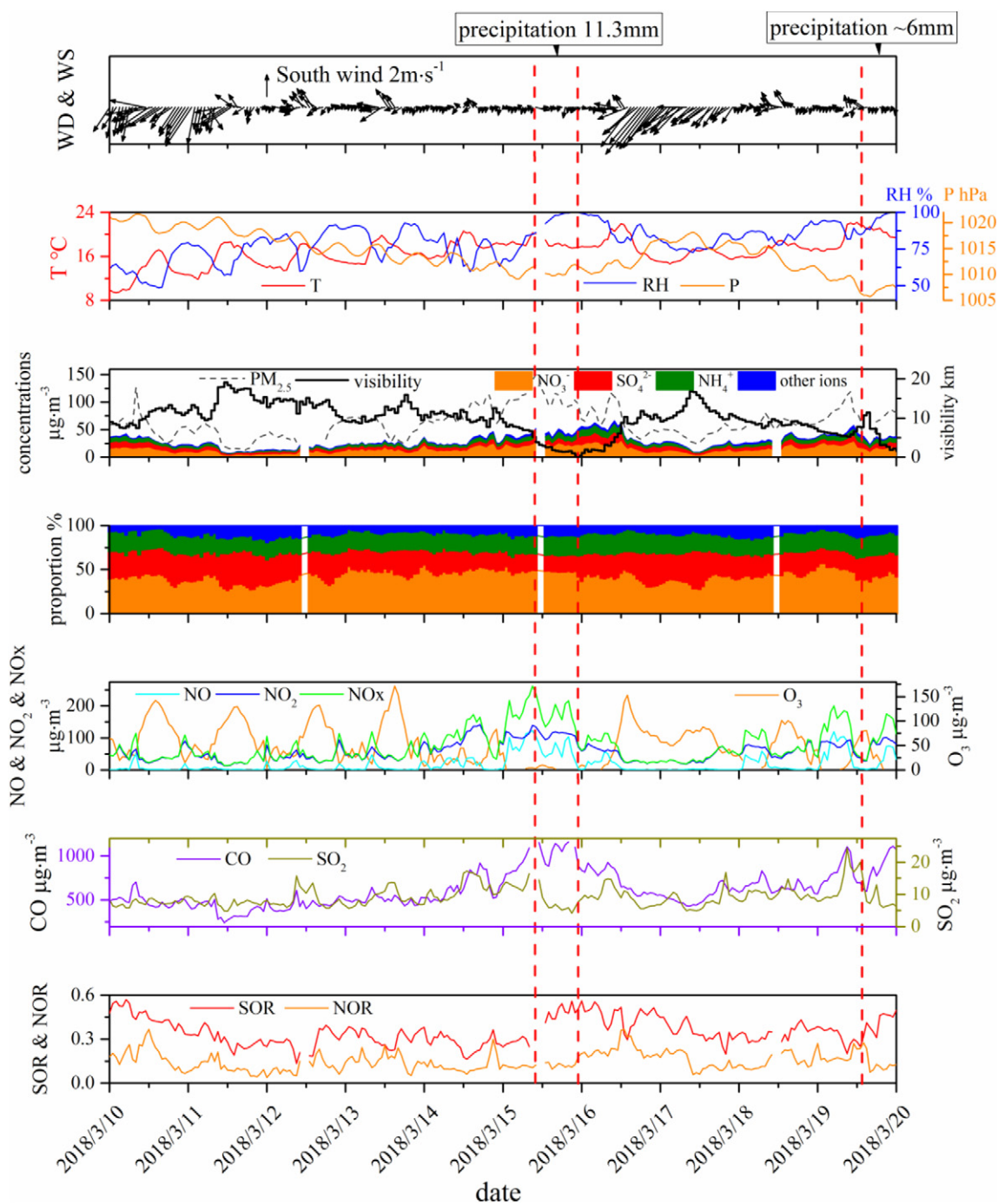
Fig. 4. Time series of surface meteorological parameters (WD, WS, T, RH and P), pollutant index (PM$_{2.5}$, visibility, WSIIs and proportions, NO-NO$_2$-NOx, O$_3$, CO and SO$_2$) and sulfur oxidation rate (SOR) and nitrogen oxidation rate (NOR).

[SO$_4^{2-}$] were at relatively high level while those in stages 2 and 4 were at lower level. The quasi-stationary front caused the humidity circumstance which possibly promoted the concentrations of [NO$_3^-$] and [NH$_4^+$].

The molar ratios of [NH$_4^+$]/[SO$_4^{2-}$] were all >2 indicating that all hourly SO$_4^{2-}$ were neutralized by NH$_4^+$. This reveals that the solid or aqueous (NH$_4$)$_2$SO$_4$ were the preferred forms of sulfate aerosol phase (Pathak et al., 2009; Squizzato et al., 2013). The molar ratios of [NO$_3^-$]/[SO$_4^{2-}$] increased with those of [NH$_4^+$]/[SO$_4^{2-}$] in four stages, so the nitrate formation may not be explained by the homogeneous gas-phase mechanisms. Pathak et al. (2009) found the nighttime heterogeneous hydrolysis of N$_2$O$_5$ on the pre-existing moist surface of nitrate aerosols.

The variations of the ratios with different RH gradients were complicated.

In the RH gradients of 79–89%, the scatters distributed widely, indicating that the heterogeneous aqueous reactions also occurred. In stages 2 and 4, when the area was governed by quasi-stationary fronts and uniform pressure field, RH, NO$_3^-$ and excess NH$_4^+$ were at higher level. The calculated concentrations of excess NH$_4^+$ were always higher than zero. It should be pointed out that all the slopes between NO$_3^-$ and excess NH$_4^+$ in the four stages were smaller than 1, which is not consistent with the molar ratio for the reaction between HNO$_3$ and NH$_3$, indicating that there were still some of excess NH$_4^+$ ions bounded to other species except NO$_3^-$, or some heterogeneous reactions resulting in the

Table 1
Summary of meteorological parameters and concentrations of chemical species in the four stages.

Parameters (units)	Stage1	Stage2	Stage3	Stage4	Average
T (°C)	13.75 ± 2.88	17.32 ± 1.90	16.34 ± 1.20	18.33 ± 2.02	16.84 ± 2.50
RH (%)	63.62 ± 9.79	82.42 ± 10.39	79.83 ± 5.41	88.34 ± 6.11	80.32 ± 11.91
WD (°)	49.9 ± 52.9	89.53 ± 99.15	46.36 ± 11.72	60.58 ± 61.26	71.34 ± 80.27
WS (m·s^{-1})	2.74 ± 0.56	0.84 ± 0.55	3.18 ± 1.07	0.82 ± 0.48	1.44 ± 1.15
P (hPa)	1019.85 ± 1.11	1013.42 ± 2.60	1015.72 ± 1.76	1010.95 ± 3.22	1014.23 ± 3.77
Vis (km)	11.73 ± 3.21	9.51 ± 4.57	11.57 ± 2.33	7.37 ± 22.35	9.90 ± 4.23
O_3 (µg·m^{-3})	69.83 ± 39.13	49.61 ± 43.05	71.09 ± 19.62	43.75 ± 30.91	55.32 ± 39.04
NO_2 (µg·m^{-3})	41.13 ± 18.17	66.81 ± 32.97	32.01 ± 14.81	66.84 ± 20.17	58.33 ± 29.84
SO_2 (µg·m^{-3})	7.39 ± 1.22	9.53 ± 3.10	7.46 ± 2.48	10.53 ± 3.76	9.14 ± 3.18
$PM_{2.5}$ (µg·m^{-3})	50.31 ± 21.09	70.65 ± 30.70	42.26 ± 9.18	67.21 ± 18.09	62.72 ± 26.92
NO_3^- (µg·m^{-3})	10.39 ± 4.53	13.29 ± 6.82	8.09 ± 3.19	15.68 ± 4.66	12.65 ± 6.14
SO_4^{2-} (µg·m^{-3})	7.77 ± 2.60	7.01 ± 3.22	6.85 ± 1.87	8.05 ± 1.30	7.34 ± 2.68
NH_4^+ (µg·m^{-3})	5.60 ± 2.37	6.27 ± 3.46	4.77 ± 1.71	7.41 ± 1.82	6.21 ± 2.92
SNA (µg·m^{-3})	23.75 ± 9.39	26.57 ± 13.08	19.46 ± 6.32	31.14 ± 7.31	26.20 ± 11.24
WSIIs (µg·m^{-3})	25.94 ± 9.78	29.45 ± 14.43	21.66 ± 6.81	34.53 ± 7.57	28.95 ± 12.28
SNA/WSIIs	0.91 ± 0.04	0.90 ± 0.03	0.91 ± 0.02	0.90 ± 0.03	0.90 ± 0.03
WSIIs/$PM_{2.5}$	0.53 ± 0.14	0.45 ± 0.17	0.51 ± 0.13	0.52 ± 0.12	0.48 ± 0.15
SNA/$PM_{2.5}$	0.49 ± 0.14	0.41 ± 0.16	0.46 ± 0.13	0.46 ± 0.11	0.45 ± 0.16
SOR	0.40 ± 0.09	0.33 ± 0.10	0.38 ± 0.08	0.35 ± 0.06	0.35 ± 0.09
NOR	0.16 ± 0.07	0.14 ± 0.06	0.17 ± 0.07	0.15 ± 0.05	0.15 ± 0.06

formation of nitrate without involving NH_3, such as heterogeneous hydrolysis of N_2O_5 during nighttime and heterogeneous conversions of NO_2 on mineral dust (Pathak et al., 2009; Seinfeld and Pandis, 2016).

4.2. Influences of aerosol acidity and LWC

Previous studies found that aerosol acidity was affected by water-soluble acidic and alkaline components directly (Zhou et al., 2012; Wu et al., 2017). The precursors of SO_2, NOx and NH_3 in the gas phase also affected acidity, as well as temperature and RH, because temperature and RH would change the rates of homogenous gaseous and heterogeneous aqueous reactions. The comparison of H_{insitu}^+ calculated by E-AIM IV and ISORROPIA II were illustrated in Fig. 6. During the whole air pollution episode, the H_{insitu}^+ derived from ISORROPIA II agreed perfectly with those from E-AIM IV ($R^2 = 0.99$), and their trends matched perfectly with each other. Therefore, the following discussion is still based on the results of E-AIM IV calculation. pH values calculated from E-AIM IV are positively correlated with that from ISORROPIA II in four stages, pH values calculated from E-AIM IV of four stages are 1.65 ± 0.21, 1.63 ± 0.31, 2.09 ± 0.36 and 1.85 ± 0.33, respectively; while those from ISORROPIA of four stages are 2.69 ± 0.32, 2.66 ± 0.14, 3.57 ± 0.24 and 2.74 ± 0.08, respectively. The differences of pH values are probably resulted from the different calculation formulas. Hydrolysis of HSO_4^- and pre-existing free H^+ in aerosols are the two constituents of H_{total}^+. Temporal variation of H_{total}^+, HSO_4^-, H_{insitu}^+ and LWC in $PM_{2.5}$ are illustrated in Fig. 7. The trends of H_{total}^+, HSO_4^- and H_{insitu}^+ are similar to each other. The total values of H_{insitu}^+ and HSO_4^- were basically

equal to H_{total}^+ revealing that the main pathways of aerosol acidity were dissolving from ions and hydrolysing from HSO_4^-.

No matter which pathway dominated the acidity, the liquid water was the key factor to derive free H^+. LWC played a vital role in heterogeneous aqueous reactions which occurred on particle surfaces. Particulate liquid water is often found to be a combined result of RH and chemical composition (Xue et al., 2014).The interactions of LWC and acidity were complicated. The correlation coefficients of LWC to H_{total}^+, HSO_4^- and H_{insitu}^+ were 0.30, 0.15 and 0.52, respectively. The release of free H^+ from HSO_4^- in the liquid phase of aerosols can enhance the acidity directly. The details of acidity and E-AIM IV output parameters in the four stages are demonstrated in Table 2. The data of LWC during the periods of precipitation were excluded. LWC, H_{total}^+ and H_{insitu}^+ are higher in stages 2 and 4 than those in stages 1 and 3. LWC probably increased H_{total}^+ and H_{insitu}^+ concentrations in stages 2 and 4, which indicated that the greater effects of LWC at the higher level on free H^+ formation than hydrolysis from HSO_4^- during the quasi-stationary front domination period. The ratios of HSO_4^- to H_{insitu}^+ could also declare the great impacts of LWC.

As shown in Fig. 8, scatters of HSO_4^-, H_{insitu}^+ and HSO_4^-/H_{insitu}^+ under different LWC values with RH gradients showed different tendencies in the four stages. The scatters of stages 1 and 3 concentrated on lower level of HSO_4^- and LWC, while the scatters of stages 2 and 4 were more discrete, which revealed that the formation mechanisms were complicated during high LWC under the influences of the quasi-stationary fronts. LWC increased with HSO_4^- and H_{insitu}^+ in different RH gradients but the slopes decreased, which indicated that the
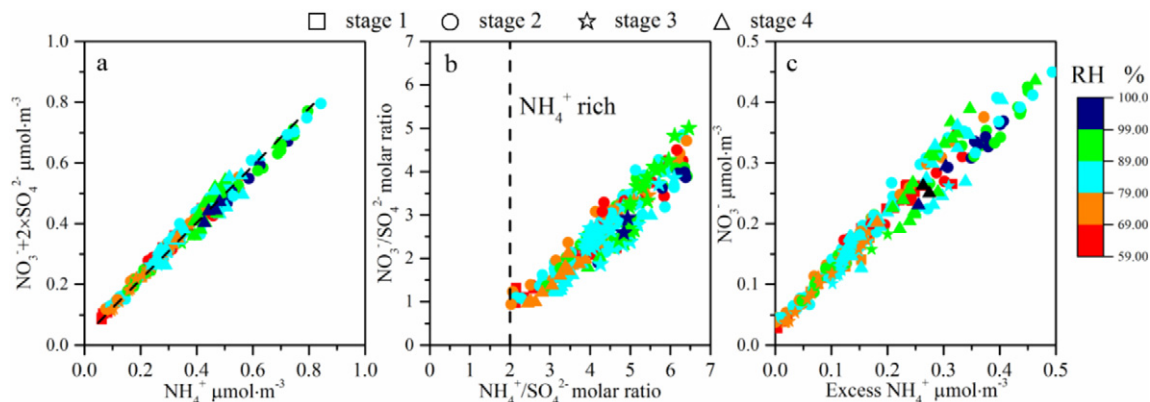

Fig. 5. Scatter plots of (a) ($NO_3^- + 2SO_4^{2-}$) vs. NH_4^+, (b) NH_4^+/SO_4^{2-} vs. NO_3^-/SO_4^{2-} and (c) NO_3^- vs. excess NH_4^+ with RH gradient in the four stages.

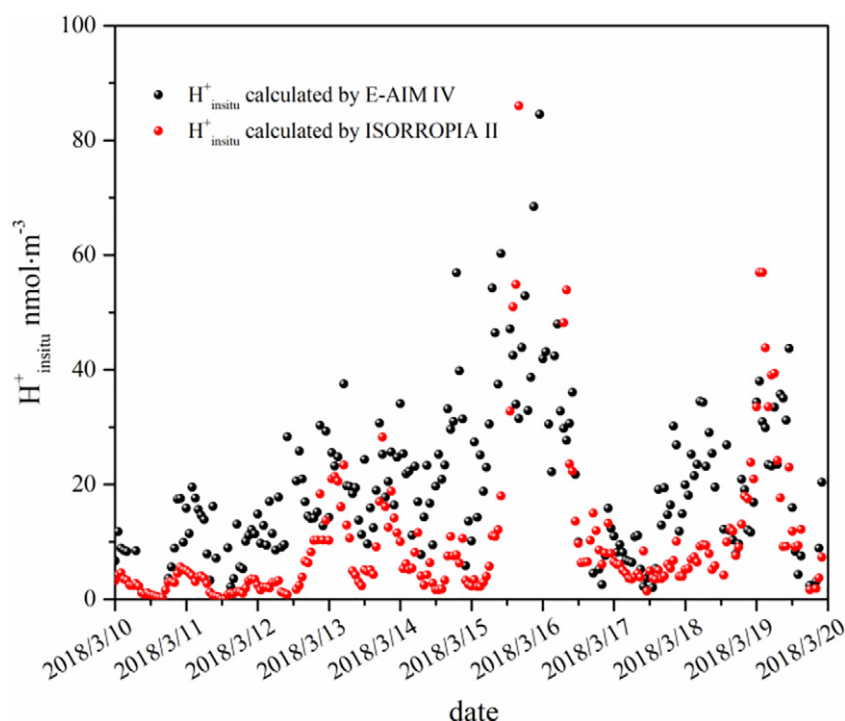**Fig. 6.** Comparison of H^+_{insitu} calculated from E-AIM IV and ISORROPIA II.

contributions of LWC to the formations of HSO_4^- and H^+_{insitu} at the higher RH levels were less than those at the lower RH levels. Although the concentrations of free H^+ hydrolyzing from HSO_4^- and in-situ H^+ of particles enhanced with LWC, the hydrolysis rates and formation rates decreased. HSO_4^-/H^+_{insitu} decreased apparently with LWC thus the hydrolysis rate was slower than that of H^+_{insitu} formations, while the contributions of hydrolysis to acidity were less than those of H^+_{insitu} formation. In stages 2 and 4 with high RH and LWC, HSO_4^-/H^+_{insitu} with minor changes were basically <2. To the contrary, HSO_4^-/H^+_{insitu} dropped sharply with low RH and LWC. The quasi-stationary fronts provided a moist environment with high LWC in particle surfaces, which possibly accelerated the formation of H^+ by the two pathways. Besides, the neutralization of acidity also delivered the similar characteristics. The

negligible HSO_4^-/H^+_{insitu} indicated that almost all the in situ acidity was neutralized, but there still existed some un-neutralized acids in total acids, being consistent with the previous studies (Huang et al., 2011).

4.3. Relationship of LWC with SNA

Previous studies have probed into the enhanced formations of the secondary aerosols in air pollution episodes, and the enhanced formation of the secondary aerosols are often thought to be ascribed to heterogeneous aqueous reactions during air pollution episodes (Hodas et al., 2014; Liu et al., 2016; Qiao et al., 2016; Wang et al., 2012; Xue et al., 2014). Particulate liquid water has important effects on the occurrence of atmospheric heterogeneous aqueous reactions by providing a
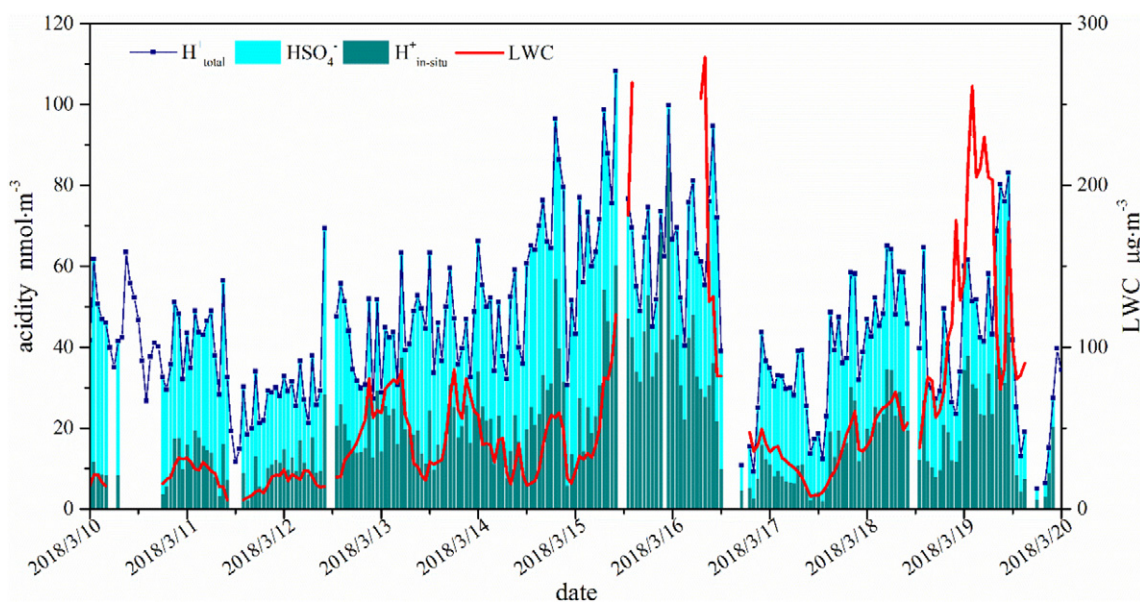

Fig. 7. Temporal variations of H^+_{total}, HSO_4^- and H^+_{insitu} in $PM_{2.5}$ during the episode.

Table 2
Parameters of acidity and E-AIM IV outputs in the four stages.

Parameters	Stage1	Stage2	Stage3	Stage4	Average
LWC $\mu g \cdot m^{-3}$	20.40 ± 7.81	50.82 ± 48.93	31.55 ± 18.66	102.66 ± 62.92	55.86 ± 53.25
H_{total}^+ $\mu mol \cdot m^{-3}$	40.43 ± 11.48	51.65 ± 19.74	30.21 ± 12.49	43.52 ± 18.29	45.49 ± 18.85
H_{insitu}^+ $\mu mol \cdot m^{-3}$	11.16 ± 4.74	24.09 ± 14.16	9.71 ± 6.48	20.91 ± 10.39	20.06 ± 13.06
HSO_4^- $\mu mol \cdot m^{-3}$	31.13 ± 7.00	27.47 ± 10.66	20.47 ± 7.03	22.87 ± 9.71	25.99 ± 10.15
HSO_4^-/H_{insitu}^+	3.40 ± 1.80	1.49 ± 0.97	2.63 ± 1.09	1.22 ± 0.47	1.80 ± 1.25

reaction medium and accelerating gas-particle transformation of gaseous pollutants, and therefore particulate liquid water plays a significant role in the formations of air pollution episodes. However, the details of the roles of the particulate liquid water in the atmosphere still remain unclear. In this study, high average RH in the four stages provided conditions for the occurrence of different heterogeneous aqueous reactions under different gradients.

To further understand the roles of heterogeneous aqueous reactions in the formation of secondary sulfate and nitrate aerosols, the relationships between SOR (NOR) and LWC with RH gradients were analyzed. SOR, NOR and visibility as a function of LWC in the four stages are illustrated in Fig. 9. A common point is clearly depicted that the scatters are discrete when RH is at the high levels, especially from 90%. SOR and LWC was nearly uncorrelated values are with the coefficient R^2 of 0.06, which manifested that LWC had no effects on the promotion of sulfate oxidation, but inhibited the sulfate formations to some extent. Previous studies have proved that the aerosol water serves as a reactor, where the alkaline aerosol components trap SO_2, which is oxidized by NO_2 to form sulfate (Cheng et al., 2016). High RH and rapidly increased fine-mode aerosol concentrations enhanced aerosol water uptake, resulting in much more LWC. Meanwhile, rich ammonia accumulated in the stagnant weather conditions significantly decreased H_{insitu}^+ (Liu et al., 2017).

Compared within the four stages, the relationships between SOR and LWC in stages 1 and 3 were more linear than those in stages 2 and 4, because of the high levels of LWC during the quasi-stationary front periods. An interesting finding was that SOR increased with LWC when SOR was <0.4 or LWC was <100 $\mu g \cdot m^3$. High nitrate episodes were believed to favor the occurrences of heterogeneous aqueous phase oxidation of SO_2, and the more water was in the particles, the more SO_2 was converted to sulfate aerosols (Kong et al., 2018). In this paper, high SO_2 and NO_2 with high concentrations of SO_4^{2-} and NO_3^- presented an evidence for more heterogeneous aqueous phase oxidations of SO_2 under the quasi-stationary front impacts.

NOR increased with LWC under different RH gradients in the four stages. However, the increasing rates of NOR under different RH reduced which demonstrated that LWC promoted nitrate oxidation with the limited RH values. A threshold value at about 100 $\mu g \cdot m^{-3}$ of LWC existed probably in heterogeneous aqueous reaction in this episode. Compared with Figs. 5 and 8, scatters in stages 2 and 4 were more

discrete than those in stages 1 and 3, indicating that relationships between LWC and formation mechanisms were intricate. Adequate LWC reflected the effect of heterogeneous aqueous reaction of NO_2 on secondary nitrate formation in this episode. Correlations between LWC and NOR in the four stages declared that heterogeneous aqueous reactions had different contributions to secondary nitrate formation, especially beyond the threshold of LWC. High concentrations of sulfate and nitrate along with the precursors of SO_2 and NO_2 were not correspondent to SOR and NOR with the high LWC. The different increasing rate of SOR and NOR to LWC implied that liquid water was more sensitive to nitrate than sulfate, which is consistent with the fact that nitrate has stronger hygroscopic ability to make particles take up water, especially at the high RH levels (Deng et al., 2016a). Furthermore, the slow rates of SO_2 and NO_2 oxidations discussed in part 3.2 and 3.3 were probably key factors to the pathways of gas phase reaction. The poor correlation between LWC and SOR could also manifest the formation mechanisms of sulfur transition.

As mentioned above, gas-phase reactions probably occurred during this episode and contributed more to the formation of sulfate and nitrate, which could explain the poor correlations between the oxidation rates and LWC. In addition, particle deliquescence might not provide adequate sulfate and nitrate although the heterogeneous aqueous reactions could still occur at the high level of LWC. Certainly, visibility reduced with RH increases obviously, which was consistent with the previous studies (Deng et al., 2016b; Wu et al., 2019). LWC, as the medium of reactions on the surfaces of particles, played a key role in the formation of sulfate and nitrate, which contributed to light extinction and led to visibility reduction. Noted that the slopes also decreased with RH gradients and LWC at the lower levels contributed more to visibility reduction, especially in stages 1 and 3 during the periods before the quasi-stationary fronts. As discussed above, formation mechanisms under the high levels of LWC were complicated and visibility decreasing rates were affected by LWC indirectly to some extent.

Positive linear regressions between SNA and RH were shown in Fig. 10. Correlations of LWC with SNA and RH are obtained by a multiple linear-regression analysis method using SPSS 17.0 statistical analysis software. The analyses report the following regression equation with an R^2 value of 0.74:

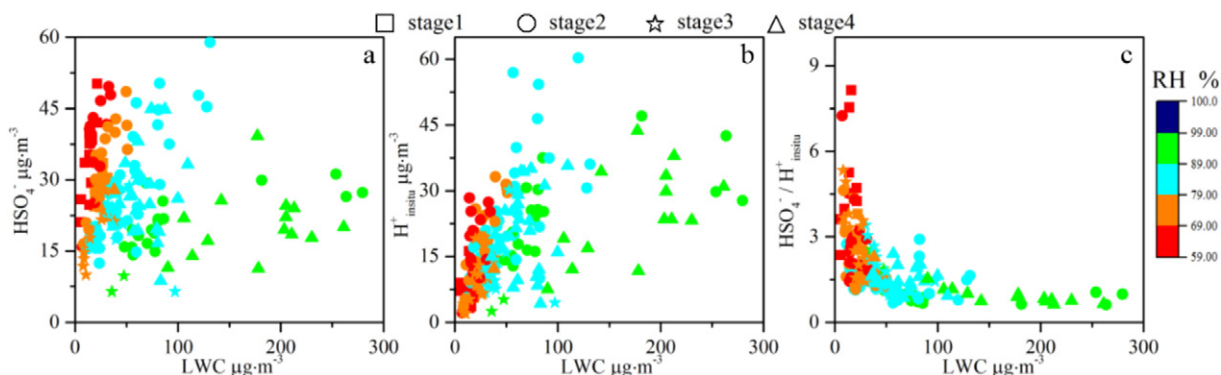$$LWC = 2.68 \times SNA + 3.62 \times RH - 300.32 \qquad (8)$$

Fig. 8. HSO_4^-, H_{insitu}^+ and HSO_4^-/H_{insitu}^+ as a function of LWC values with RH gradients in the four stages.

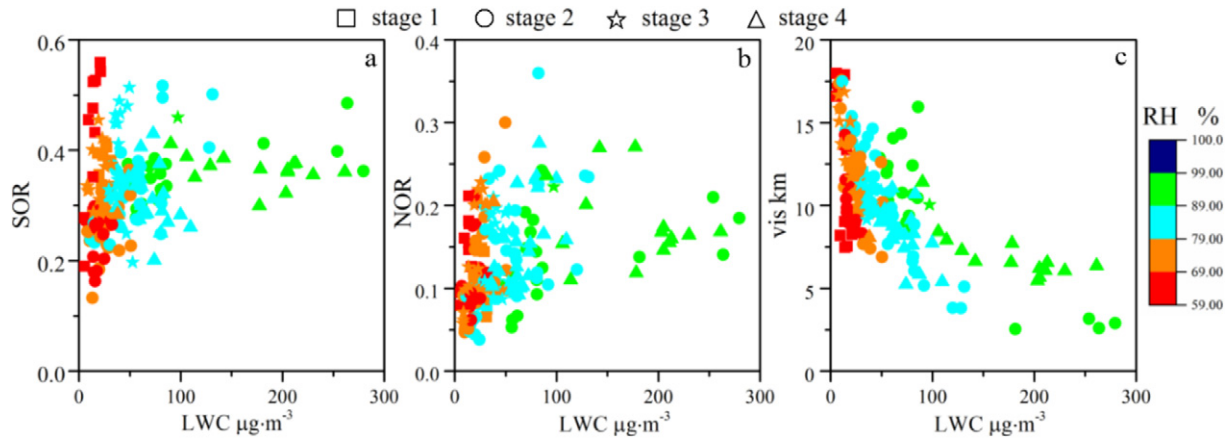**Fig. 9.** Scatter plots of SOR, NOR and visibility as a function of LWC under RH gradients.

where both LWC and SNA are in $\mu g \cdot m^{-3}$ and RH is in %. The high correlation reveals that LWC of aerosols collected during different periods can be well explained by RH and SNA concentrations. The empirical nature of the relationship makes it difficult to attribute a physical meaning to the intercept. Mathematically, the magnitude of the intercept, i.e., 300.32 in Eq. (6), corresponds to the sum of $(2.68 \times SNA + 3.62 \times RH)$ when the aerosols are totally crystallized and no LWC exists. In situations of no LWC, SNA values are in the ranges of 9–17 $\mu g \cdot m^{-3}$ and RH values are in the ranges of 0.4–0.59, thereby giving rise to a large intercept of -300. This finding prompts us to carry out a multiple linear-regression analysis with sulfate and nitrate as separate input variables, which yields Eq. (9) with an R^2 value of 0.98:

$$LWC = 4.49 \times [NH_4NO_3] + 0.78 \times [(NH_4)_2SO_4] + 3.58 \times RH - 291.51 \tag{9}$$

where $[(NH_4)_2SO_4]$ and $[NH_4NO_3]$ are concentrations in $\mu g \cdot m^{-3}$. Here, sulfate is assumed to exist in the form of $(NH_4)_2SO_4$ and nitrate in NH_4NO_3 based on the high correlation between $[NH_4^+]$ and $2[SO_4^{2-}]$- $+ [NO_3^-]$ in Fig. 8. p-Values of 0.01 (<0.05) are obtained for coefficients associated with $(NH_4)_2SO_4$, NH_4NO_3 and RH, indicating the results are considered statistically significant. NH_4NO_3 was the driving force of

the enhanced LWC. NH_4NO_3 formation under excess NH_3 induced the decreasing of relative humidity for aerosol deliquescence and accelerated the hygroscopic growth. A further increase of RH promotes the positive feedback to heterogeneous reactions and ultimately leads to the formation of air pollution (Ge et al., 2019).

4.4. Photolysis rates of NO$_2$

In addition, $J_{(NO2)}$ and UV data were applied in this study to show evidence for the oxidations rate variations during this episode. As depicted in Fig. 11, time series of $J_{(NO2)}$ and UV appeared nearly same tendencies which indicated that the atmospheric radiation was weak during some periods with the high levels of $PM_{2.5}$ and low visibility when compared with Fig. 3. It is noted that the oxidation reactions occurred sharply when the radiation was intensive. $J_{(NO2)}$ and UV decreased in 14th and 15th March when $PM_{2.5}$ increased, which revealed that NO_2 participated in the homogeneous gas phase and/or heterogeneous aqueous reactions rather than the photo-chemical reactions. In general, heterogeneous aqueous reactions occurred when the atmospheric radiation was at the low level. Therefore, the results together with those discussed in Sections 4.1 and 4.2 suggested an important contribution of the heterogeneous aqueous reactions to secondary aerosols. The air
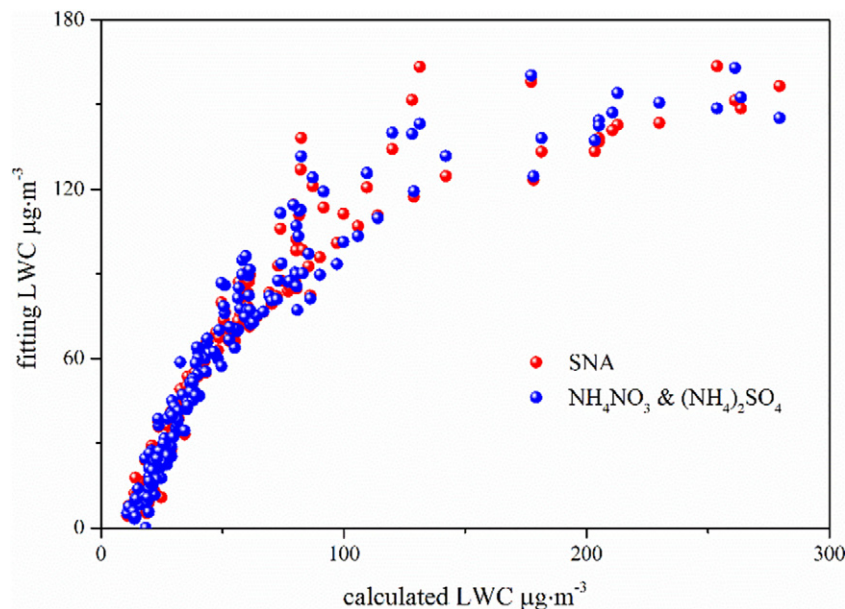

Fig. 10. Scatter plot of calculated LWC as a function of fitting LWC from Eqs. (6) and (7).
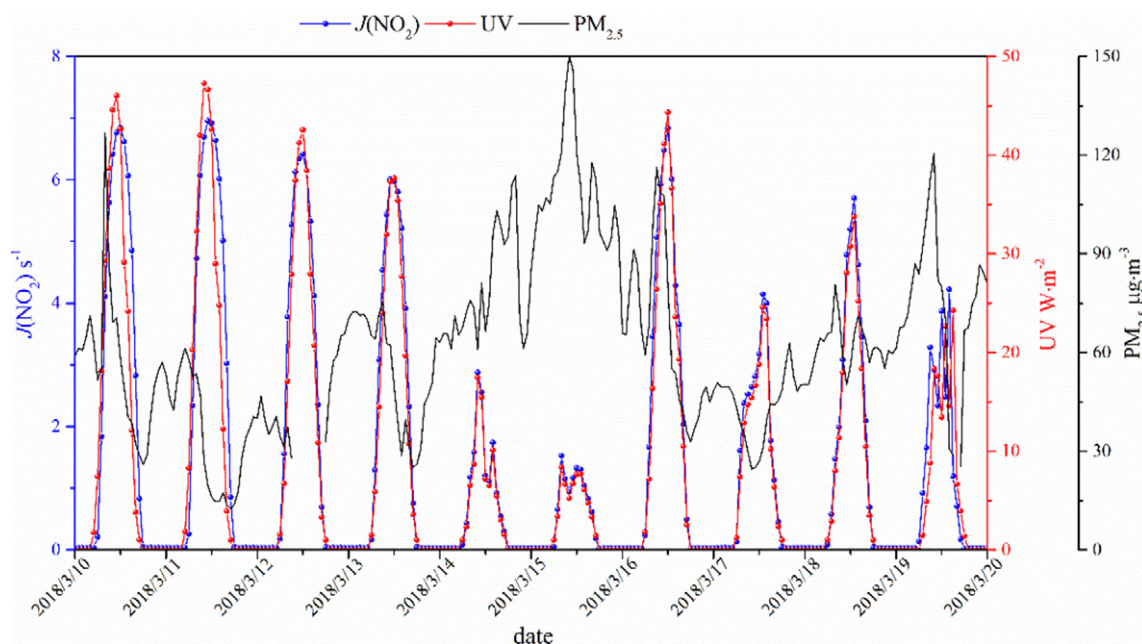
Fig. 11. Evolution of $J(NO_2)$, UV and $PM_{2.5}$ during the air pollution episode.

pollution episode occurred during the quasi-stationary fronts was a complicated secondary pollution episode with both homogeneous gaseous and heterogeneous aqueous reaction processes (Park et al., 2016a, 2016b; Tie et al., 2017).

5. Conclusions

In this paper, an air pollution episode induced by the quasi-stationary front was diagnosed. The synoptic charts, MODIS images and backward trajectories results revealed the quasi-stationary front impacts on Xiamen cities. The characteristics of the four divided stages according to the locations of quasi-stationary fronts were analyzed to elucidate the formation mechanisms of secondary pollution. The secondary pollution could be ascribed to local pollution and synoptic situation impact. This air pollution episode was defined as a high-nitrate episode which was governed by nitrate inherently. Further discussions indicated that $PM_{2.5}$ had strong acidity and adequate liquid water content during the air pollution episode when they were calculated by E-AIM IV. It was also found that liquid water in aerosols was more sensitive to nitrate than sulfate, and played a vital role in the heterogeneous aqueous reactions of NO_2 and secondary nitrate formation during the episode. Homogeneous gaseous reaction also occurred with the low values of sulfur oxidation rate and nitrogen oxidation rate. In addition, the evolutions of $J_{(NO2)}$ and UV declared that NO_2 participated in the homogeneous gas phase and/or heterogeneous aqueous reactions rather than the photo-chemical reactions when $PM_{2.5}$ concentration increased.

Declaration of competing interest

The authors declare that there is no conflict of financial interest.

References

Bei, N., Li, G., Huang, R.J., Cao, J., Meng, N., Feng, T., Liu, S., Zhang, T., Zhang, Q., Molina, L.T., 2016. Typical synoptic situations and their impacts on the wintertime air pollution in the Guanzhong basin, China. Atmos. Chem. Phys. 16, 7373–7387. https://doi.org/10.5194/acp-16-7373-2016.

Bougiatioti, A., Nikolaou, P., Stavroulas, I., Kouvarakis, G., Weber, R., Nenes, A., et al., 2016. Particle water and pH in the eastern Mediterranean: source variability and implications for nutrient availability. Atmos. Chem. Phys. 16, 4579–4591.

Chen, Z.H., Cheng, S.Y., Li, J.B., Guo, X.R., Wang, W.H., Chen, D.S., 2008. Relationship between atmospheric pollution processes and synoptic pressure patterns in northern China. Atmos. Environ. 42, 6078–6087.

Cheng, Y.F., Zheng, G.J., Wei, C., 2016. Reactive nitrogen chemistry in aerosol water as a source of sulfate during haze events in China. Sci. Adv., e1601530

Clegg, S.L., Brimblecombe, P., Wexler, A.S., 1998. Thermodynamic model of the system H+-NH4+-SO42-NO3-H2O at tropospheric temperatures. J. Phys. Chem. A 102, 2137–2154.

Davis, R.E., Kalkstein, L.S., 1990. Using a spatial synoptic climatological classification to assess changes in atmospheric pollution concentrations. Phys. Geogr. 11, 320–342.

Deng, H., Tan, H., Li, F., Cai, M., Chan, P.W., Xu, H., et al., 2016a. Impact of relative humidity on visibility degradation during a haze event: a case study. Sci. Total Environ. 569-570, 1149–1158.

Deng, J.J., Zhang, Y.R., Hong, Y.W., Xu, L.L., Chen, Y.T., Du, W.J., Chen, J.S., 2016b. Optical properties of PM2.5 and the impacts of chemical compositions in the coastal city Xiamen in China. Sci. Total Environ. 557–558, 665–675.

Fountoukis, C., Nenes, A., 2007. ISORROPIA II: a computationally efficient thermodynamic equilibrium model for K+ – Ca2+ – Mg2+ – NH4+ – Na+ – SO42− –NO3− –Cl− – H2O aerosols. Atmos. Chem. Phys. 7, 4639–4659.

Friese, E., Ebel, A., 2010. Temperature dependent thermodynamic model of the system H+-NH4+-Na+-SO42−-NO3−-Cl−-H2O. J. Phys. Chem. A 114, 11595–11631.

Ge, B., Sun, Y., Liu, Y., Dong, H., Ji, D., Jiang, Q., Li, J., Wang, Z., 2013. Nitrogen dioxide measurement by cavity attenuated phase shift spectroscopy (CAPS) and implications in ozone production efficiency and nitrate formation in Beijing, China. J. Geophys. Res. Atmos. 118, 9499–9509. https://doi.org/10.1002/jgrd.50757.

Ge, B., Xu, X., Ma, Z., Pan, X., Wang, Z., Lin, W., et al., 2019. Role of ammonia on the feedback between AWC and inorganic aerosol formation during heavy pollution in NCP. Earth and Space Science 6. https://doi.org/10.1029/2019EA000799.

Greene, J.S., Kalkstein, L.S., Ye, H., Smoyer, K., 1999. Relationships between synoptic climatology and atmospheric pollution at 4 US cities. Theor. Appl. Climatol. 62, 163–174.

Guo, H., Sullivan, A.P., Campuzano-Jost, P., Schroder, J.C., Lopez-Hilfiker, F.D., Dibb, J.E., et al., 2016. Fine particle pH and the partitioning of nitric acid during winter in the northeastern United States. J. Geophys. Res. Atmos. 121, 10355–10376.

Hodas, N., Sullivan, A.P., Skog, K., Keutsch, F.N., Collett Jr., J.L., Decesari, S., et al., 2014. Aerosol liquid water driven by anthropogenic nitrate: implications for lifetimes of

water-soluble organic gases and potential for secondary organic aerosol formation. Environ. Sci. Technol. 48, 11127–11136.

Huang, X., Qiu, R., Chan, C.K., Ravi Kant, P., 2011. Evidence of high $PM_{2.5}$ strong acidity in ammonia-rich atmosphere of Guangzhou, China: transition in pathways of ambient ammonia to form aerosol ammonium at $[NH_4^+]/[SO_4^{2-}]$ = 1.5. Atmos. Res. 99, 488–495.

Kalkstein, L.S., Corrigan, P.R., 1986. A synoptic climatological approach for geographical analysis: assessment of sulfur dioxide concentrations. Ann. Assoc. Am. Geogr. 76, 381–395.

Kaneyasu, N., Ohta, S., Murao, N., 1995. Seasonal variation in the chemical composition of atmospheric aerosols and gaseous species in Sapporo, Japan. Atmos. Environ. 29, 1559–1568.

Kong, L.D., Du, C.T., Assiya, Z., Cheng, T.T., Yang, X., Wang, L., Fu, H.B., Chen, J.M., Zhang, S.C., 2018. Trends in heterogeneous aqueous reaction in continuous haze episodes in suburban Shanghai: an in-depth case study. Sci. Total Environ. 634, 1192–1204.

Li, P.F., Yan, R.C., Yu, S.C., Wang, S., Liu, W.P., Bao, H.M., 2015. Reinstate regional transport of PM2.5 as a major cause of severe haze in Beijing. Proc Natl Acad Sci USA (PNAS) 112 (21), E2739–E2740. https://doi.org/10.1073/pnas.1502596112.

Li, N., Tang, G.Q., Zhao, P., Hong, Y., Gou, Y.B., Yang, K., 2017. Statistical assessment and hydrological utility of the latest multi-satellite precipitation analysis IMERG in Ganjiang River basin. Atmos. Res. 183, 212–223.

Liu, Z., Hu, B., Zhang, J., Yu, Y., Wang, Y., 2016. Characteristics of aerosol size distributions and chemical compositions during wintertime pollution episodes in Beijing. Atmos. Res. 168, 1–12.

Liu, M.X., Song, Y., Zhou, T., et al., 2017. Fine particle pH during severe haze episodes in northern China. Geophys. Res. Lett. 44, 5213–5221. https://doi.org/10.1002/2017GL073210.

Park, S.S., Kim, Y.J., 2004. PM2.5 particles and size-segregated ionic species measured during fall season in three urban sites in Korea. Atmos. Environ. 38, 1459–1471.

Park, S.S., Cho, S.Y., Jung, C.H., Lee, K.H., 2016a. Characteristics of water-soluble inorganic species in PM10 and PM2.5 at two coastal sites during spring in Korea. Atmos. Pollu. Res. 7, 370–383.

Park, S.S., Cho, S.Y., Jung, C.H., Lee, K.H., 2016b. Characteristics of water-soluble inorganic species in PM_{10} and $PM_{2.5}$ at two coastal sites during spring in Korea. Atmos. Pollu. Res. 7, 370–383.

Pathak, R.K., Wu, W.S., Wang, T., 2009. Summertime PM2.5 ionic species in four major cities of China: nitrate formation in an ammonia-deficient atmosphere. Atmos. Chem. Phys. 9, 1711–1722.

Pope, C.A.I.I.I., 2000. Review: epidemiological basis for particulate air pollution health standards. Aerosol Sci. Technol. 32, 4–14.

Qiao, T., Zhao, M., Xiu, G., Yu, J., 2016. Simultaneous monitoring and compositions analysis of PM1 and PM 2.5 in Shanghai: implications for characterization of haze pollution and source apportionment. Sci. Total Environ. 557-558, 386–394.

Ramanatha, V., Crutzen, P.J., Kiehl, J.T., Rosenfeld, D., 2001. Aerosol climate and hydrological cycle. Science 294, 2119–2124.

Seinfeld, J.H., Pandis, S.N., 2016. Atmospheric Chemistry and Physics: From Air Pollution to Climate Change. John Wiley & Sons.

Squizzato, S., Masiol, M., Brunelli, A., Pistollato, S., Tarabotti, E., Rampazzo, G., et al., 2013. Factors determining the formation of secondary inorganic aerosol: a case study in the Po Valley (Italy). Atmos. Chem. Phys. 13, 1927–1939.

Sun, Y., Zhuang, G., Tang, A., Wang, Y., An, Z., 2006. Chemical characteristics of PM2.5 and PM10 in haze-fog episodes in Beijing. Environ. Sci. Technol. 40, 3148–3155.

Tian, M., Wang, H., Chen, Y., Zhang, L., Shi, G., Liu, Y., et al., 2017. Highly time-resolved characterization of water-soluble inorganic ions in PM2.5 in a humid and acidic mega city in Sichuan Basin, China. Sci. Total Environ. 580, 224–234.

Tie, X.X., Huang, R.J., Cao, J.J., Zhang, Q., Cheng, Y.F., Su, H., Chang, D., Pöschl, U., Hoffmann, T., Dusek, U., Li, G.H., Worsnop, D.R., O'Dowd, C.D., 2017. Severe pollution in China amplified by atmospheric moisture. Sci. Rep. 7, 15760.

Trebs, I., Meixner, F.X., Slanina, J., Otjes, R., Jongejan, P., Andreae, M.O., 2004. Real-time measurements of ammonia, acidic trace gases and water-soluble inorganic aerosol species at a rural site in the Amazon Basin. Atmos. Chem. Phys. 4, 967–987.

Wang, Y.Q., Zhang, X.Y., Draxler, R.R., 2009. Traj Stat: GIS-based software that uses various trajectory statistical analysis methods to identify potential sources from long-term air pollution measurement data. Environ. Model. Softw. 24, 938–939. https://doi.org/10.1016/j.envsoft.2009.01.004.

Wang, X., Wang, W., Yang, L., Gao, X., Nie, W., Yu, Y., Xu, P., Zhou, Y., Wang, Z., 2012. The secondary formation of inorganic aerosols in the droplet mode through heterogeneous aqueous reactions under haze conditions. Atmos. Environ. 63, 68–76.

Wang, G., Zhang, R., Gomez, M.E., Yang, L., Zamora, M.L., Hu, M., et al., 2016a. Persistent sulfate formation from London Fog to Chinese haze. Proc. Natl. Acad. Sci. U. S. A. 113, 13630–13635.

Wang, H.L., Qiao, L.P., Lou, S.R., Zhou, M., Ding, A.J., Huang, H.Y., et al., 2016b. Chemical composition of PM2.5 and meteorological impact among three years in urban Shang- hai, China. J. Clean. Prod. 112, 1302–1311.

Wang, L.J., Wang, C., Guo, D., 2018. Evolution mechanism of synoptic-scale EAP teleconnection pattern and its relationship to summer precipitation in China. Atmos. Res. 214, 150–162.

Wang, Y.L., Song, W., Yang, W., Sun, X.C., Tong, Y.D., Wang, X.M., 2019. Influences of atmospheric pollution on the contributions of major oxidation pathways to PM2.5 nitrate formation in Beijing. J. Geophys. Res. Atmos. 124, 4174–4185. https://doi.org/10.1029/2019JD030284.

Watson, J.G., 2002. Visibility: science and regulation. J. Air Waste Manage. Assoc. 52, 628–713.

Wu, X., Deng, J.J., Chen, J.S., Hong, Y.W., Xu, L.L., Yin, L.Q., Du, W.J., Hong, Z.Y., Dai, N.Z., Yuan, Chung-Shin, 2017. Characteristics of water-soluble inorganic components and acidity of PM2.5 in a coastal city of China, Aerosol Air Qual. Res., 17(9), 2152–2164.

Wu, X., Xu, L.L., Hong, Y.W., Chen, J.F., Qiu, Y.Q., Hu, B.Y., Hong, Z.Y., Zhang, Y.R., Liu, T.T., Chen, Y.T., Bian, Y.H., Zhao, G.Q., Chen, J.S., Li, M.R., 2019. The air pollution governed by subtropical high in a coastal city in Southeast China: formation processes and influencing mechanisms. Sci. Total Environ. 692, 1135–1145.

Xue, J., Griffith, S.M., Yu, X., Lau, A.K.H., Yu, J.Z., 2014. Effect of nitrate and sulfate relative abundance in PM2.5 on liquid water content explored through half-hourly observations of inorganic soluble aerosols at a polluted receptor site. Atmos. Environ. 99, 24–31.

Yan, Y., Fu, P.Q., Jing, B., Peng, C., Boreddy, S.K.R., Yang, F., Wei, L.F., Sun, Y.L., Wang, Z.F., Ge, M.F., 2017. Hygroscopic behavior of water-soluble matter in marine aerosols over the East China Sea. Sci. Total Environ. 578, 307–316.

Zhang, X.Y., Wang, J.Z., Wang, Y.Q., Liu, H.L., Sun, J.Y., Zhang, Y.M., 2015. Changes in chemical components of aerosol particles in different haze regions in China from 2006 to 2013 and contribution of meteorological factors. Atmos. Chem. Phys. 15, 12935–12952.

Zhao, M., Huang, Z., Qiao, T., Zhang, Y., Xiu, G., Yu, J., 2015a. Chemical characterization, the transport pathways and potential sources of PM2.5 in Shanghai: seasonal variations. Atmos. Res. 158-159, 66–78.

Zhao, M., Qiao, T., Huang, Z., Zhu, M., Xu, W., Xiu, G., Tao, J., Lee, S., 2015b. Comparison of ionic and carbonaceous compositions of PM2.5 in 2009 and 2012 in Shanghai, China. Sci. Total Environ. 536, 695–703.

Zhou, Y., Xue, L.K., Wang, T., Gao, X.M., Wang, Z., Wang, X.F., Zhang, J.M., Zhang, Q.Z., Wang, W.X., 2012. Characterization of aerosol acidity at a high mountain site in central eastern China. Atmos. Environ. 51, 11–20.